https://doi.org/10.26599/FRICT.2026.9441307

Research Article

Reverse micelles as nanocarriers for polar friction modifiers in non-polar oils: AOT-mediated solubilization and boundary film formation

Haiyang Gu[1,*], Tomoko Hirayama[1,*], Lin Sun[1], Masako Yamada[2]

1. *Department of Mechanical Engineering and Science, Graduate School of Engineering, Kyoto University, Katsura, Nishikyo-ku, Kyoto 615–8540, Japan*
2. *Neutron Science Division, Institute of Materials Structure Science, KEK, 203–1 Shirakata, Tokai-village, Naka-gun, Ibaraki 319–1106, Japan*

*Corresponding author: gu.haiyang.4v@kyoto-u.ac.jp, tomoko@me.kyoto-u.ac.jp

Received: July 27, 2026; Revised: August 17, 2026; Accepted: September 2, 2026

Abstract

Polar organic friction modifiers can form effective boundary-lubrication films, but their limited compatibility with non-polar oils restricts their delivery to sliding interfaces. In this study, LCC was selected as a model polar additive to evaluate the ability of AOT reverse micelles in n-dodecane to act as nanocarriers for oil-incompatible friction modifiers. Increasing the water-to-surfactant molar ratio, *w*, expanded the transparent solubilization range of the model additive and increased the hydrodynamic size of the reverse micellar aggregates. Neutron reflectometry showed that hydrated AOT aggregates formed an adsorbed layer at the FeO_x/oil interface, and incorporation of the model additive increased the fitted adsorbed-layer thickness from 3.05 to 3.43 nm under the same fixed-SLD fitting condition. Ball-on-disk tests showed lower friction after additive incorporation, and XPS detected chlorine-containing LCC-derived species on the

worn surfaces, indicating that LCC was delivered to and retained at the sliding interface. Molecular dynamics simulations were used to observe the structural response of additive-loaded reverse micelles under high-pressure shear. These results support a reverse-micelle-assisted delivery mechanism in which hydrated AOT aggregates solubilize polar additives in the bulk oil, adsorb at the interface, and release additive-derived species under sliding.

Keywords: Reverse micelles; AOT; Boundary lubrication; Neutron reflectometry; Molecular dynamics; Additive release

1. Introduction

Friction and wear consume a substantial fraction of useful mechanical energy and shorten the service life of moving components [1–3]. Lubricants mitigate these losses by separating contacting surfaces, removing heat, and controlling chemical reactions at interfaces. In boundary lubrication, where the fluid film is thin and asperity contact becomes important, performance depends strongly on the additives that adsorb, react, or assemble at the sliding interface [4–6].

Non-polar and weakly polar base oils are widely used because they combine good chemical stability with favorable volatility, oxidation resistance, and viscosity-temperature behavior [7–9]. These properties are valuable in high-temperature or long-duration applications. However, the same low polarity that gives these oils their stability also limits their ability to dissolve many functional additives. This limitation is especially important for additives whose activity depends on polar or ionic groups.

Organic friction modifiers illustrate this dilemma clearly. Their polar headgroups can promote adsorption on metal or oxide surfaces and help organize low-shear boundary films [10–12]. Their hydrocarbon chains, meanwhile, provide compatibility with the oil phase and can contribute to ordered interfacial packing. A molecule that is too non-polar may dissolve well but adsorb weakly, whereas a molecule with a strong polar headgroup may adsorb effectively but disperse poorly in non-polar oils. Lubricant formulation therefore faces a coupled solubility and delivery problem.

Conventional strategies address this problem in two main ways. The first is to change the solvent environment, for example by blending non-polar base oils with more polar ester components [13,14]. This can increase the apparent solubility of polar additives and improve tribological response. The second is to redesign additive molecules so that they are intrinsically oil-soluble while retaining surface activity [15,16]. Both approaches are useful, but they also introduce formulation constraints. Solvent blending changes the base-oil composition, and molecular redesign must be repeated for each additive family.

A carrier-based strategy offers a different route for decoupling bulk-phase compatibility from interfacial function. In our previous study, we introduced the concept of “additive encapsulation” in aqueous lubrication, in which surfactant micelles functioned as dynamic, self-assembled additive capsules [17]. Sodium 2-hexyldecanoate (2HDNa) micelles were used to incorporate palmitic acid, a poorly water-soluble model friction modifier, into an aqueous lubricant at concentrations far above its intrinsic solubility. Palmitic acid could be incorporated at concentrations of up to 0.4 wt%, corresponding to more than 500 times its intrinsic solubility in water. FTIR and SAXS confirmed that palmitic acid was incorporated within the micellar

aggregates without chemical conversion, while tribological tests showed a maximum friction reduction of more than 33%. Combined QCM-D and neutron reflectometry results supported a mechanism in which the micelles transport the encapsulated additive to the solid–liquid interface and deform under contact pressure, thereby making the additive available for boundary-film formation [17]. The significance of this strategy is therefore not limited to lowering the coefficient of friction; it provides a formulation route for solubilizing, transporting, and utilizing functional additives that are otherwise incompatible with the base fluid.

By regulating the spatial availability of additives, encapsulation may also reduce unnecessary exposure in non-contact regions and thereby mitigate undesirable side effects such as corrosion, while organizing additives into nanoscale aggregates could potentially facilitate future separation or removal strategies under increasingly stringent environmental regulations; these broader possibilities, however, remain to be experimentally verified.

The present study extends this additive-encapsulation strategy from aqueous normal micelles to reverse micelles in non-polar oils. In reverse micelles, the surfactant headgroups form an internal polar domain, while the hydrocarbon tails interact with the surrounding oil phase. This reversed molecular organization enables a polar or ionic additive to be incorporated within a nanoscale hydrated environment while the overall aggregate remains dispersible in a non-polar base oil. Sodium bis(2-ethylhexyl) sulfosuccinate (AOT) reverse micelles are a well-established model system because they can incorporate water, swell with increasing water-to-surfactant molar ratio, w, and provide tunable polar nanodomains in apolar solvents [18–20].

For lubrication, however, bulk solubilization alone is insufficient. A useful carrier must remain dispersed in the oil, reach or adsorb at the solid–liquid interface, and release the incorporated additive under tribological loading. Our previous study inferred pressure-assisted additive release from interfacial and tribological observations, but the dynamic structural response of the carrier during sliding was not directly resolved. AOT reverse micelles are known to undergo structural changes under shear [21], but this behavior has not been directly connected to additive release and interfacial retention in a lubricant system. The present study therefore examines the complete delivery sequence from bulk solubilization and static interfacial adsorption to shear-induced carrier disruption, additive release, and retention of additive-derived species on the worn surface.

In this study, n-dodecane was selected as a model non-polar base oil, AOT was used to form reverse micelles, and lauroyl choline chloride (LCC) was introduced as a polar model friction modifier. LCC was selected in the present study as a deliberately simple and analytically traceable model additive. It consists of a permanently charged quaternary-ammonium choline headgroup and a C12 acyl chain, giving it a polar-head/hydrocarbon-tail motif common to surface-active organic additives. Its ionic character provides a stringent test of compatibility with non-polar n-dodecane, while the chloride counterion serves as an element-specific XPS marker absent from the AOT/dodecane formulation. Accordingly, LCC was employed not as a benchmark commercial friction modifier, but as a chemically defined probe for evaluating reverse-micelle-mediated solubilization, interfacial delivery, and release.

We first examined how *w* controls LCC solubilization and reverse micellar size by visual inspection and dynamic light scattering (DLS). We then used neutron reflectometry (NR) to determine whether the reverse micellar aggregates adsorb at FeOx-coated solid-liquid interfaces and whether LCC incorporation changes the adsorbed layer. Ball-on-disk tests and

X-ray photoelectron spectroscopy (XPS) were used to connect the carrier structure to friction reduction and the presence of LCC-derived species on the worn surface. Finally, MD simulations were used to observe the missing dynamic step: deformation and disruption of LCC-loaded reverse micelles under high-pressure shear and release of LCC from the original polar cores.

2. Experimental

2.1. Materials

Dodecane (purity >99%, Tokyo Chemical Industry Co., Ltd.) was used as the non-polar model base oil without further purification. Sodium bis(2-ethylhexyl) sulfosuccinate (AOT, BioXtra grade, purity >=99%, Sigma-Aldrich) was used as the surfactant. Lauroyl choline chloride (LCC, purity >98.0%, Tokyo Chemical Industry Co., Ltd.) was used as the polar model friction modifier. The molecular structures of AOT and LCC are shown in Fig. 1.

For NR experiments, deuterated n-dodecane (d-dodecane-d26, isotopic purity >98%, Cambridge Isotope Laboratories) was used to enhance neutron scattering contrast. Deuterium oxide (D_2O, 99.9 atom % D, Sigma-Aldrich) was used as the aqueous component for contrast-variation measurements.

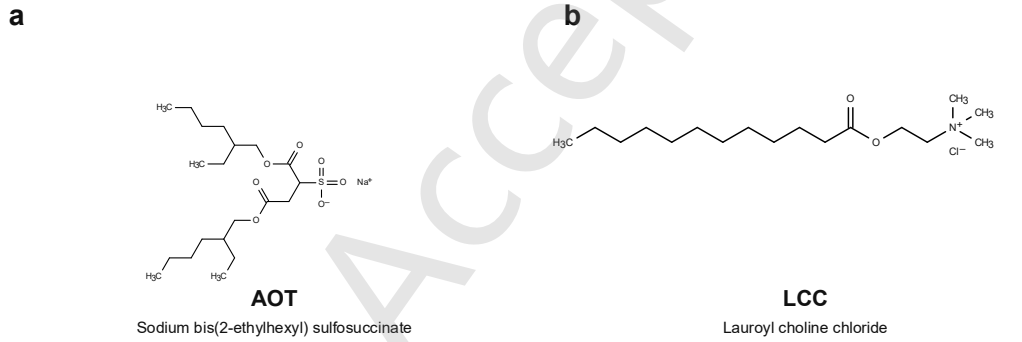

Fig. 1. Chemical structures of AOT and LCC.

2.2. Dynamic light scattering

DLS measurements were conducted to evaluate the hydrodynamic size of AOT reverse micellar aggregates in n-dodecane at w = 5, 10, and 20. Measurements were performed at room temperature using a Zetasizer Nano ZS90 instrument (Malvern Instruments). Prior to analysis, each sample was sonicated for 10 min to ensure uniform dispersion. After sonication, the samples were equilibrated at room temperature and then transferred to the measurement cell. For each composition, at least three independent measurements were performed to confirm the reproducibility of the obtained size distributions. The hydrodynamic diameter of the reverse micelles was determined from the autocorrelation data using the cumulant analysis method.

2.3. Neutron reflectometry

Neutron reflectometry (NR) measurements were carried out to investigate the interfacial adsorption behavior of reverse micellar structures and the effect of additive incorporation on the adsorbed layer at the solid–liquid interface [22–25]. The measurements were performed using the SOFIA horizontal-type neutron reflectometer installed at the Materials and Life

Science Experimental Facility (MLF), J-PARC, Japan [26].

Highly polished silicon blocks (50 × 50 × 10 mm) were used as substrates for the NR experiments. Each substrate was coated with an Fe layer with a thickness of approximately 30 nm by ion beam sputtering using the KUR-IBS system [27]. The Fe-coated silicon block was mounted in a liquid cell, allowing solution exchange while maintaining the relative alignment between the substrate and the instrument.

In the first set of measurements, reverse micellar solutions composed of AOT in dodecane at a fixed water-to-surfactant molar ratio of w=5 were examined to evaluate the adsorption behavior of the reverse micelles themselves. To provide neutron scattering contrast for the water core of the reverse micelles, two types of samples were prepared using either H_2O or D_2O as the aqueous phase. Reflectivity profiles obtained from these two contrast conditions were compared to analyze the interfacial structure of the adsorbed reverse micellar layer.

In the second set of measurements, NR was used to assess the influence of LCC on the interfacial adsorption behavior of the AOT reverse micellar system. Reflectivity profiles were first measured for the AOT reverse micellar solution without LCC, and the corresponding data were used as a reference. Subsequently, the AOT solution containing LCC was introduced into the same cell, and the reflectivity profile was measured again. The structural changes induced by the addition of LCC were evaluated by comparing the fitted interfacial parameters before and after LCC incorporation.

All measurements were conducted at incident angles of 0.3°, 0.6°, and 1.2° over a wavelength range of 0.20–0.88 nm. The reflectivity profiles were constructed by combining the data collected at the different incident angles. The momentum transfer normal to the interface (Q_z) ranged from 0 to 0.12 $Å^{-1}$. The neutron footprint on the sample surface was maintained at 40 × 40 mm throughout the measurements.

The reflectivity data were analyzed using GenX 3 software [28]. A multilayer model consisting of the Si substrate, native SiO_2 layer, Fe layer, FeO_x layer, and adsorbed layer was employed for fitting. For the analysis, the structural parameters of the substrate-side layers, including thickness and scattering length density (SLD), were first determined and then fixed during subsequent fitting procedures. The thickness, SLD, and roughness of the adsorbed layer were refined to evaluate the interfacial structure of the reverse micellar systems and the effect of LCC addition.

2.4. Tribology tests

Reciprocating friction tests were performed on a ball-on-disk tribometer (FPR-2100, RHESCA Co. Ltd., Japan) under boundary lubrication conditions at a controlled temperature of 23 °C. The force-detection system of the FPR-2100 has a resolution of 1/20000 of full scale, corresponding to 0.25 gf (approximately 2.45 mN). Polished SUS304 stainless-steel disks (surface roughness Ra ≈ 0.04 μm, dimensions 10 × 10 × 2 mm) and SUS440C stainless-steel balls (Ra ≈ 0.04 μm, diameter 3/16 inch) were employed as the sliding counterparts. Before each test, both disks and balls were sequentially cleaned by ultrasonication in acetone and hexane for 5 min to remove surface contaminants. Detailed experimental parameters used in the tribological measurements are summarized in Table 1.

Each tribological condition was independently repeated 3 times. The average coefficient of friction for each test was calculated over the final 200 s, corresponding to the final 200 cycles

of the test. The reported COF values represent the mean values of the independent measurements, and the error bars indicate the corresponding standard deviations.

Table 1. Tribology test conditions

Parameter	Value
Normal load (N)	1.96
Temperature (°C)	23
Stroke distance (mm)	5
Frequency (Hz)	1
Cycles	600

2.5. X-ray photoelectron spectroscopy

XPS was used to analyze the chemical composition of the tribofilms formed on the wear tracks. After the friction tests, the disk specimens were gently rinsed with hexane to remove excess lubricant, dried under a stream of nitrogen, and then stored in a sealed vacuum container until analysis.

XPS measurements were performed using a PHI VersaProbe 4 instrument equipped with a monochromatic Al Kα X-ray source (hv = 1486.6 eV). Survey spectra were acquired with a pass energy of 224 eV, and high-resolution spectra for Fe 2p, O 1s, C 1s, S 2p and Cl 2p were collected with a pass energy of 55 eV. Charge neutralization was applied during acquisition. All binding energies were calibrated by setting the main C 1s peak of adventitious carbon to 284.8 eV. Background subtraction was carried out using a Shirley-type background, and peak fitting was performed with mixed Gaussian–Lorentzian line shapes to evaluate the chemical states of sulfur- and chlorine-containing species in the tribofilms formed with and without LCC at different *w*.

2.6. Molecular dynamics simulations

Molecular dynamics (MD) simulations were performed using GROMACS 2025.4 [29]. The confined shear model consisted of two Fe_2O_3 hematite (0001) slabs, hereafter referred to as FeO_x substrates, and a reverse-micelle-containing lubricant phase confined between them, as shown in Fig. 2. The lateral box dimensions of the lubricant phase were fixed to match those of the FeO_x substrate, namely 15.11 × 14.83 nm^2. The system contained 120 AOT^-, 120 Na^+, 600 TIP3P water molecules, and 3600 dodecane molecules, which were preassembled into three reverse micelles. Each reverse micelle contained 40 AOT^-, 40 Na^+, and 200 water molecules, corresponding to w = [water]/[AOT] = 5. For the LCC-containing system, 18 LCC^+ and 18 Cl^- were additionally introduced, corresponding to an initial loading of 6 LCC^+ and 6 Cl^- per reverse micelle. Dodecane molecules were packed around the preassembled reverse micelles using Packmol [30].

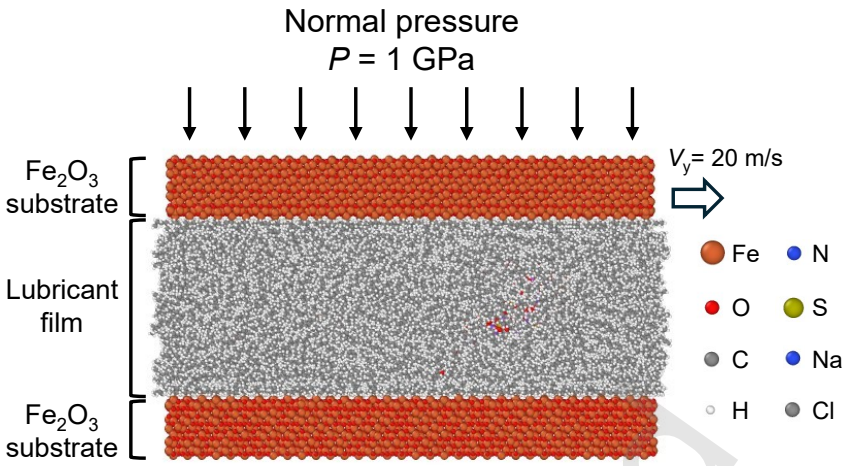

Fig. 2. Confined MD simulation model used to observe reverse micelle disruption and LCC release under high-pressure shear.

Force-field parameters compatible with OPLS-AA were used for the organic species [31]. The topologies of dodecane and LCC^+ were generated using LigParGen [32]. For AOT^-, the bonded parameters were retained from the LigParGen-generated topology, whereas the partial charges and selected Lennard-Jones parameters for the sulfonate/headgroup region were taken from previously reported AOT parameters [33]. Water was described using the TIP3P model [34], and Na^+ and Cl^- were described using the GROMACS OPLS-AA ion parameters. The FeO_x substrates were described using the same non-reactive fixed-charge model in all simulations.

The lubricant phase was first pre-equilibrated as an independent liquid box. The x and y dimensions of the liquid box were fixed to the lateral dimensions of the FeO_x substrate, while pressure coupling was applied only along the z direction. The initial lubricant structure was sequentially subjected to steepest-descent energy minimization without bond constraints, energy minimization with LINCS constraints applied to bonds involving hydrogen atoms [35], 20 ps NVT pre-equilibration, and 5 ns z-only NPT equilibration. A time step of 1 fs was used during the NVT and NPT stages. The temperature was maintained at 298.15 K using the velocity-rescale thermostat [36]. During the z-only NPT equilibration, the C-rescale barostat was used with semi-isotropic pressure coupling [37], where the compressibility in the x/y directions was set to 0 and that in the z direction was set to 4.5×10^{-5} bar^{-1}. This allowed the box length to relax only in the surface-normal direction while keeping the lateral dimensions fixed.

The equilibrated lubricant phase was then inserted between two FeO_x slabs, and its position along the surface-normal direction was adjusted so that the minimum initial distance between the lubricant phase and the upper and lower FeO_x surfaces was approximately 0.4 nm. The confined system was subsequently subjected to energy minimization without bond constraints, energy minimization with LINCS constraints applied to bonds involving hydrogen atoms, 50 ps NVT equilibration, and a 5 ns normal loading process. During both energy-minimization steps, position restraints were applied to the controlled layers of the FeO_x slabs to avoid nonphysical displacement of the substrates. No pressure coupling was applied during the NVT equilibration or the loading stage of the confined system, and the temperature was maintained at 298.15 K. In each 40,800-atom FeOx slab, the outer backing layer contained 5,100 atoms

(2,040 Fe and 3,060 O). The backing layer of the lower slab was harmonically restrained in all three Cartesian directions with a force constant of 100,000 kJ mol^{-1} nm^{-2} and served as the fixed reference group. The remaining 35,700 atoms of the lower slab were mobile. The corresponding 5,100-atom backing layer of the upper slab was not position-restrained during sliding, but was used as the driven group to which the normal force and the moving lateral reference potential were applied. The remaining atoms of the upper slab, including both lubricant-facing surface regions, were allowed to move.

Normal loading and sliding were implemented using the GROMACS pull code. The lower FeO_x slab was used as the fixed reference group, while the upper FeO_x slab was used as the driven group. During the loading process, the lower FeO_x substrate was kept fixed, and a constant external force was applied to the upper FeO_x substrate along the surface-normal direction to impose a nominal normal pressure of approximately 1 GPa. Long-range electrostatic interactions were treated using the particle mesh Ewald (PME) method. Short-range nonbonded interactions were truncated at 1.2 nm, and slab correction was applied for the confined interfacial systems. The shear simulations were performed under an equivalent normal pressure of 1 GPa and a sliding velocity of 20 m s^{-1} for 50 ns. Based on the lateral area of the substrate, a normal pressure of 1 GPa corresponds to a constant normal force of 224.17 nN, equivalent to 135000 kJ mol^{-1} nm^{-1} in GROMACS units, which was applied using constant-force pulling. Sliding was imposed along the y direction, and a velocity of 20 m s^{-1} corresponds to a pull rate of 0.020 nm ps^{-1}. Based on the time-averaged confined-film thickness, the corresponding nominal geometric shear rate was calculated as 3.8×10^{9} s^{-1}. For long-duration, large-displacement shear simulations under high pressure, the direction-periodic pulling geometry was used to avoid nonphysical displacement jumps caused by periodic boundary conditions. During shear, the lubricant, lower FeOx slab, and upper FeOx slab were coupled separately to a velocity-rescale thermostat at 298.15 K with a coupling time constant of 1.0 ps. All three Cartesian kinetic degrees of freedom were thermostatted, and no direction-selective thermostat was applied. Bonds involving hydrogen atoms were constrained using LINCS. Separate temperature-coupling groups were used to dissipate shear-generated heat without applying a single global thermal bath to the lubricant and both substrates. Center-of-mass velocity removal was disabled to preserve the externally imposed sliding motion, and no pressure coupling was applied during shear.

The structural evolution of the reverse micelles during the 50 ns shear trajectories was characterized by the radius of gyration, shape anisotropy, AOT-water aggregate size, water-core integrity, and water-core radius. The initial identity of each reverse micelle was assigned based on the initial water-core/AOT distribution and was tracked throughout the simulation. The release behavior of LCC^{+} was evaluated using the LCC^{+}-AOT contact number, the LCC^{+}-sulfonate contact number, and the distance between the LCC^{+} headgroup and the instantaneous center of the polar core of the corresponding reverse micelle. The first analyzed frame at 0.5 ns was used to assign the initial identities of the three reverse micelles based on periodic clustering of water oxygen atoms, and these assignments were retained throughout the analysis. The retained fraction was defined using a cutoff of 3.2 nm from the instantaneous center of the corresponding tracked water core. Cluster connectivity was defined using a minimum-image pair-distance cutoff of 0.8 nm, and the largest-cluster fraction was calculated as the number of nodes in the largest connected component divided by the total number of assigned nodes.

LCC^{+}–AOT and LCC^{+}–sulfonate contacts were defined using a cutoff of 0.6 nm under minimum-image periodic boundary conditions.

3. Results and discussion

3.1. Solubilization behavior of LCC in AOT reverse micellar solutions

Fig. 3 shows the visual appearance of LCC-containing 50 mM AOT/dodecane solutions at different water-to-surfactant molar ratios (w = 0, 2, and 5), providing direct evidence for the solubilization behavior of LCC in AOT reverse micellar media. A clear dependence on water content was observed. In the nominally anhydrous system (w = 0), the solutions remained transparent up to 0.2 wt% LCC, whereas obvious turbidity appeared at 0.3 wt%, indicating that the solubilization limit had been exceeded. The limited solubilization of LCC at w = 0 is likely attributable to trace amounts of water originally present in the oil phase or surfactant, or introduced during sample preparation and handling. Such residual water can provide small hydrated polar domains within AOT aggregates, allowing a limited amount of the polar additive to be incorporated even without intentional water addition. When a small amount of water was intentionally introduced (w = 2), the transparent region expanded and homogeneous solutions were maintained up to 0.5 wt% LCC, while further addition to 0.6 wt% resulted in loss of clarity. A further increase in water content to w = 5 enhanced the solubilization capacity even more, with transparent solutions observed up to 0.7 wt% LCC, whereas the sample containing 0.8 wt% LCC showed visible phase instability. These results demonstrate that the solubilization capacity of the AOT reverse micellar solution increased monotonically with increasing w.

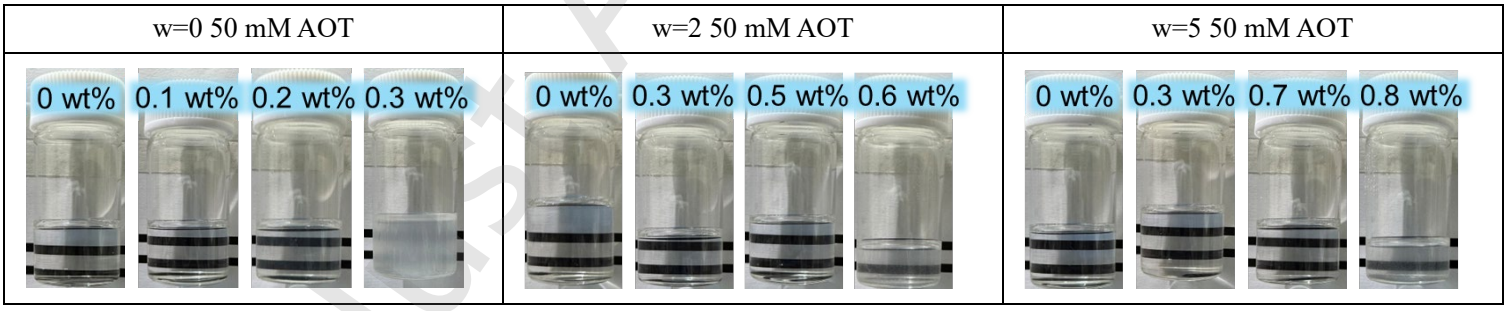

Fig. 3. Solubilization behavior of LCC in AOT reverse micellar solutions.

This trend is consistent with the structural characteristics of AOT reverse micelles in nonpolar solvents. In the absence of added water, the polar cores of the reverse micelles are highly limited, and LCC can only be incorporated to a small extent through interactions with the sulfosuccinate headgroups of AOT. As w increases, water molecules are incorporated into the reverse micellar cores, leading to enlargement of the polar domain and creation of a more favorable microenvironment for LCC. Because LCC is an amphiphilic and highly polar ionic compound, its incorporation is expected to be promoted by the presence of hydrated reverse micellar interiors, where electrostatic interactions, ion–dipole interactions, and hydrogen-bonding interactions can collectively stabilize the solubilized state. The progressive increase in the maximum transparent LCC concentration from 0.2 wt% at w = 0 to 0.5 wt% at w = 2 and 0.7

wt% at w = 5 strongly supports this interpretation. Water-containing AOT reverse micelles can function as effective carriers for introducing otherwise poorly oil-soluble ionic additives into nonpolar lubricating media.

3.2. Structural characterization of reverse micelles

To better understand the origin of the enhanced LCC solubilization described in Section 3.1, the structure of the AOT reverse micellar systems was examined by DLS. Fig. 4a shows the representative hydrodynamic size distributions of 50 mM AOT reverse micelles in n-dodecane at different water contents, while Fig. 4b summarizes the corresponding average hydrodynamic diameters. In all cases, a single dominant distribution was observed, indicating the formation of relatively well-defined reverse micellar aggregates within the measured composition range. More importantly, the distribution shifted systematically toward larger diameters with increasing w, demonstrating progressive growth of the reverse micellar structure upon water addition. It should be noted that the DLS distributions are intensity-weighted; therefore, the observed change reflects a shift of the dominant hydrodynamic size toward larger values rather than simply an increase in the number of aggregates of the same size. The convergence toward a single dominant peak suggests that one characteristic aggregate population increasingly dominates the scattering response.

Quantitatively, the average hydrodynamic diameter increased from approximately 16 nm at w = 5 to about 42 nm at w = 10, and further to around 108 nm at w = 20. This marked size increase clearly indicates that added water substantially changes the organization of AOT aggregates in the nonpolar medium. Such behavior is consistent with the well-established tendency of AOT reverse micelles to swell as water is incorporated into their polar interiors. As the amount of solubilized water increases, the internal polar domain becomes larger, and the overall hydrodynamic size of the aggregate increases accordingly. The relatively narrow unimodal distributions observed here further suggest that the systems remained structurally stable and did not undergo extensive macroscopic phase separation under these conditions.

When considered together with the solubilization results in Fig. 3, the DLS data provide a structural explanation for the improved LCC incorporation at higher w. In Section 3.1, the maximum concentration of LCC that could be visually solubilized increased significantly with increasing water content. The present DLS results indicate that increasing w produces larger reverse micellar aggregates with expanded polar interiors, which would be expected to provide a more accommodating microenvironment for LCC.

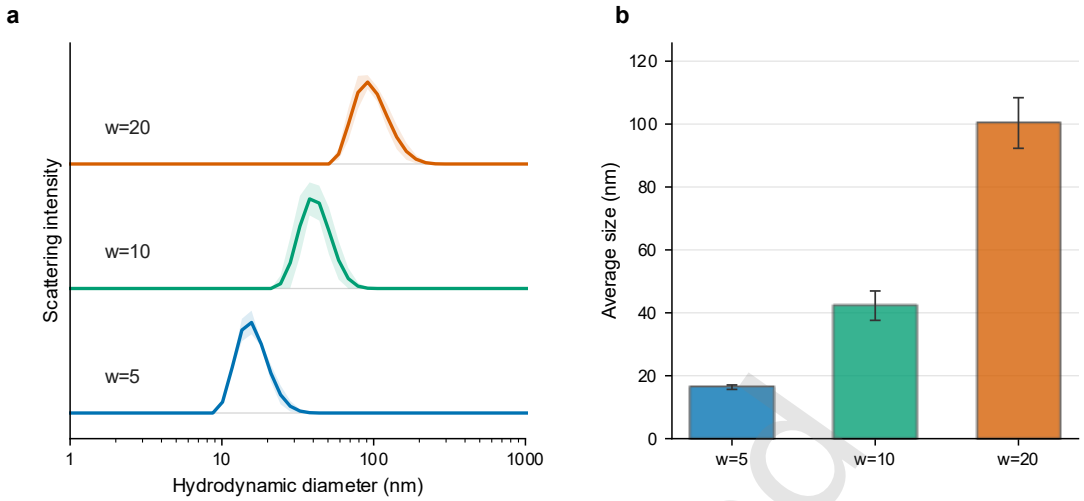

Fig. 4. DLS analysis of AOT reverse micellar systems. (a) Representative hydrodynamic size distributions of AOT reverse micelles in n-dodecane at different *w* values. (b) Average hydrodynamic diameter of the reverse micelles as a function of *w*. The error bars represent the standard deviation from repeated measurements.

3.3. Adsorption behavior of AOT reverse micelles at the solid–liquid interface

To determine whether AOT reverse micelles remained only in the bulk oil phase or also contributed to interfacial film formation, neutron reflectometry (NR) measurements were performed for 50 mM AOT/d-dodecane solutions at w = 5 using either H_2O or D_2O as the aqueous phase. The experimental and fitted reflectivity curves are shown in Fig. 5. In the figure, the triangles represent the experimental NR data, whereas the solid black lines correspond to the fitted reflectivity profiles. The darker curves represent the *d*-dodecane-only baseline, while the upper curves correspond to the AOT reverse micellar solutions. Compared with the d-dodecane baseline, the AOT solutions showed clear changes in the reflectivity profiles. These changes could be reasonably described only by including an additional interfacial layer in the fitting model, indicating the formation of an AOT-derived adsorbed layer at the solid–liquid interface. Importantly, the reflectivity profiles of the H_2O- and D_2O-containing systems were clearly different over the measured Q_z range, although the surfactant concentration and oil phase composition were otherwise identical.

The fitted parameters obtained using a model with the layer thickness fixed at 4.10 nm are summarized in Table 2. Under this fitting constraint, the SLD was determined to be 2.73×10^{-6} Å^{-2} for the H_2O-based sample and 4.67×10^{-6} Å^{-2} for the D_2O-based sample. The substantial difference in fitted SLD demonstrates that the interfacial layer is sensitive to isotopic substitution of the water incorporated in the reverse micelles. Since the only intentional difference between the two samples was the use of H_2O or D_2O as the aqueous phase, this contrast-dependent behavior strongly indicates that the adsorbed layer contains a water-related component derived from the reverse micellar interior.

When combined with the solubilization and DLS results, increasing w promoted both the growth of the reverse micelles in the bulk phase and the incorporation of polar species, while the NR results show that these water-containing assemblies also participate in interfacial adsorption. Thus, the adsorbed layer is more reasonably interpreted as a reverse-micelle-

derived hydrated interfacial film, which is likely to be highly relevant to the subsequent lubrication behavior.

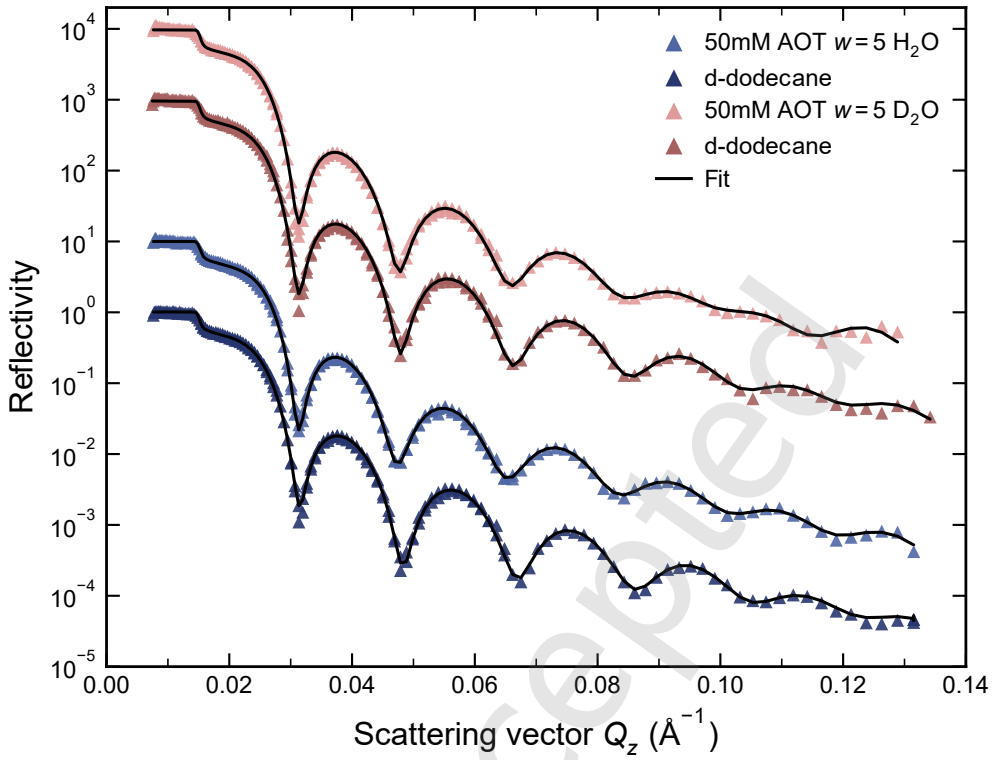

Fig. 5. Neutron reflectometry analysis of the adsorption behavior of AOT reverse micelles. Experimental and fitted neutron reflectivity curves of AOT reverse micellar solutions at $w = 5$ prepared with H_2O or D_2O as the aqueous phase.

Table. 2. Fitted NR parameters of AOT reverse micellar adsorbed layers with H_2O and D_2O contrasts.

Sample	Thickness / nm	SLD / $\times 10^{-6}$ Å^{-2}
AOT (w = 5, H_2O) in d-dodecane	4.10	2.73
AOT (w = 5, D_2O) in d-dodecane	4.10	4.67

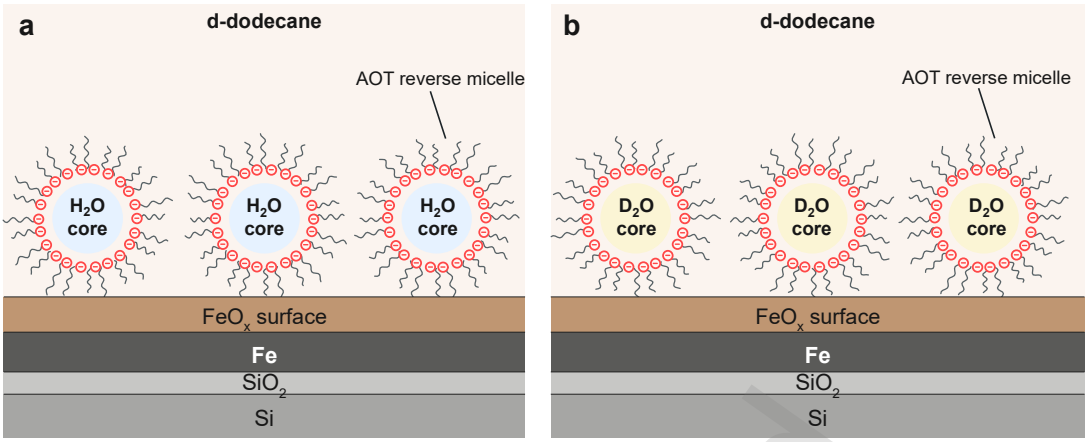

Fig. 6. Schematic illustration of NR contrast variation for AOT reverse micelles with H_2O and D_2O cores adsorbed at the FeOx/d-dodecane interface.

3.4. Tribological performance of LCC-containing reverse micellar systems

The tribological performance of the LCC-containing reverse micellar systems was evaluated by ball-on-disk friction tests, and the representative friction coefficient (COF) curves are shown in Fig. 7a–d. The corresponding average COF values are summarized in Fig. 7e. In the absence of LCC, the AOT reverse micellar systems showed a clear dependence on the water-to-surfactant molar ratio, w (Fig. 7a). The anhydrous AOT solution ($w = 0$) exhibited an average COF of approximately 0.164, while the $w = 2$ system showed a slightly lower value of approximately 0.143. In contrast, the $w = 5$ system displayed the highest COF, approximately 0.189, together with larger fluctuations during sliding. These results indicate that hydration of the reverse micelles alone does not necessarily improve lubrication, and excessive hydration may even deteriorate the friction behavior in the absence of the polar additive.

After incorporation of LCC as a model polar additive, the COF decreased for all examined w values compared with the corresponding LCC-free AOT systems. For the anhydrous system ($w = 0$), addition of 0.2 wt% LCC reduced the average COF from approximately 0.164 to 0.132, corresponding to a friction reduction of 19.3%.

At $w = 2$, the LCC-free AOT reverse micellar solution showed an average COF of approximately 0.143. Upon addition of LCC, the COF decreased to approximately 0.128 at 0.3 wt% LCC and further to approximately 0.123 at 0.5 wt% LCC. The maximum friction reduction relative to the LCC-free system was 13.7%. Although the percentage reduction was smaller than that observed for $w = 0$, the absolute COF values were lower, indicating that moderate hydration facilitates the friction-reducing action of the incorporated polar additive.

A more pronounced concentration dependence was observed for the $w = 5$ system. The LCC-free sample exhibited the highest average COF among the AOT-only systems, approximately 0.189. However, increasing the LCC concentration progressively reduced friction, giving average COF values of approximately 0.147, 0.133, 0.129, and 0.123 for 0.1, 0.3, 0.5, and 0.7 wt% LCC, respectively. The maximum friction reduction reached 35.0% relative to the corresponding LCC-free sample. This clear concentration-dependent improvement indicates that highly hydrated reverse micelles can accommodate and utilize larger amounts of the polar additive, although the hydrated AOT aggregates themselves are not intrinsically beneficial for friction reduction.

Overall, the friction results demonstrate that the lubrication performance of the AOT/LCC reverse micellar system is governed by both the hydration level of the reverse micelles and the concentration of the incorporated polar additive. Hydration expands the additive-solubilization capacity of the reverse micelles, while the incorporated LCC provides the primary friction-reducing contribution. Therefore, effective lubrication requires an appropriate balance between reverse micelle hydration and polar additive loading.

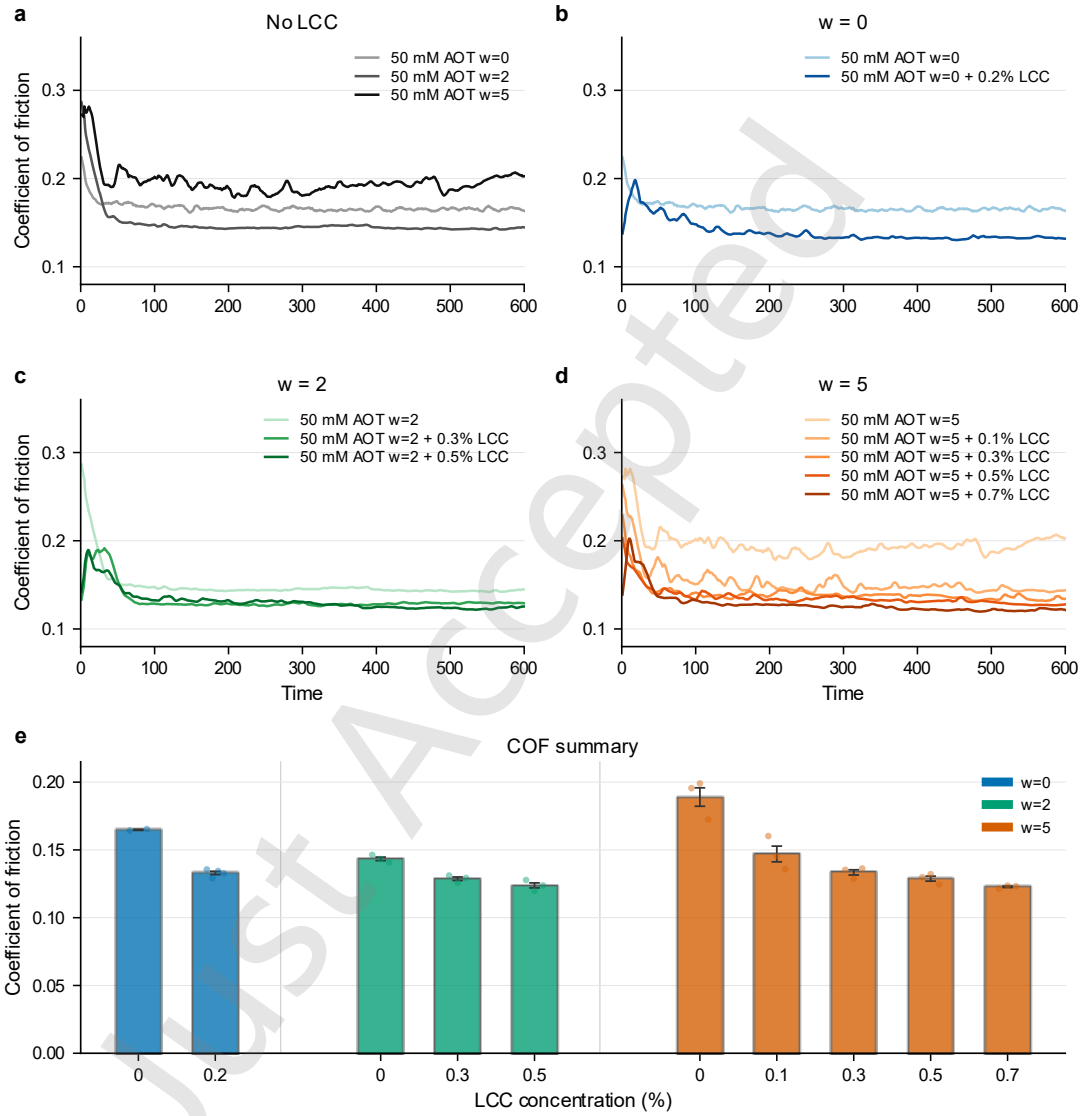

Fig. 7. Tribological performance of LCC-containing AOT reverse micellar solutions in n-dodecane. Representative COF curves are shown for (a) LCC-free AOT systems at different *w* values, (b) the *w* = 0 system, (c) the *w* = 2 system, and (d) the *w* = 5 system, (e) Summary of the corresponding average COF values. Data in panel (e) are presented as the mean ± standard deviation of three independent tests. For each test, the COF was averaged over the final 200 s, corresponding to the final 200 cycles.

3.5. Effect of LCC on interfacial adsorption behavior

To further examine how incorporation of LCC affects the interfacial adsorption structure, neutron reflectometry (NR) measurements were carried out for the AOT reverse micellar

system before and after the addition of LCC. These measurements were performed at w=0. The experimental and fitted reflectivity curves are shown in Fig. 8, where the triangles represent the experimental data and the solid black lines represent the fitted profiles. After the addition of LCC, the reflectivity fringes shifted systematically toward lower Qz. According to the Bragg relation, this shift indicates an increase in the characteristic thickness of the adsorbed interfacial layer.

For the second NR analysis, the SLD of the adsorbed layer was fixed at 3.3×10^{-6} Å^{-2}. In the fitting model used here, this value corresponds to an effective adsorbed-layer density of 50%. The SLD and thickness of an interfacial layer are strongly correlated in NR fitting, and different combinations of these parameters can reproduce the experimental reflectivity with comparable fitting quality. Therefore, when both parameters are varied independently, the fitting solution is not necessarily unique. The primary purpose of the second NR experiment was to compare the interfacial layer before and after LCC addition rather than to determine an absolute SLD independently for each sample. Accordingly, the layer SLD was constrained to the same value of 3.3×10^{-6} Å^{-2} for both datasets, while the layer thickness was allowed to vary. This common-SLD treatment reduces the number of free parameters and enables a direct comparison of the effective layer thickness under an identical contrast assumption.

The fitted SLD profiles are shown in Fig. 9, and the corresponding fitted thickness values are summarized in Table 3. For direct comparison, the SLD was fixed at 3.3×10^{-6} Å^{-2} during fitting, corresponding to an assumed density of 50%. Under this fitting condition, the thickness of the adsorbed layer increased from 3.05 nm for the 50 mM AOT system to 3.43 nm after the addition of 0.2 wt% LCC. This corresponds to an increase of 0.38 nm, or approximately 12.5%, quantitatively demonstrating that incorporation of LCC led to thickening of the interfacial adsorption layer.

Because the fitting was performed using the same fixed SLD for both samples, the difference in fitted thickness directly reflects a structural change in the adsorbed layer rather than a variation in the assumed layer density. As shown in Section 3.3, the AOT reverse micelles adsorb at the solid–liquid interface as intact aggregates. Therefore, the increase in adsorption-layer thickness observed here can be reasonably attributed to an increase in reverse micelle size after incorporation of LCC. This interpretation is consistent with the leftward shift of the reflectivity fringes shown in Fig. 8.

A schematic illustration of this structural change is shown in Fig. 10. Before the addition of LCC, AOT reverse micelles form an adsorbed interfacial layer with a thickness of approximately 3.05 nm. After incorporation of LCC, the adsorbing reverse micelles become larger, resulting in an increase in the thickness of the interfacial layer to 3.43 nm. Thus, the NR results indicate that the addition of LCC increases the size of the reverse micellar aggregates and correspondingly modifies the thickness of the adsorbed layer at the interface.

It should be noted that the NR measurements described above were conducted under static conditions and therefore mainly reflect the equilibrium interfacial structure before friction. To clarify how the additive-containing reverse micellar system behaves under actual sliding conditions, further analysis of the worn surfaces after tribological testing is required. For this reason, XPS measurements were performed on the wear tracks, as discussed in the next section.

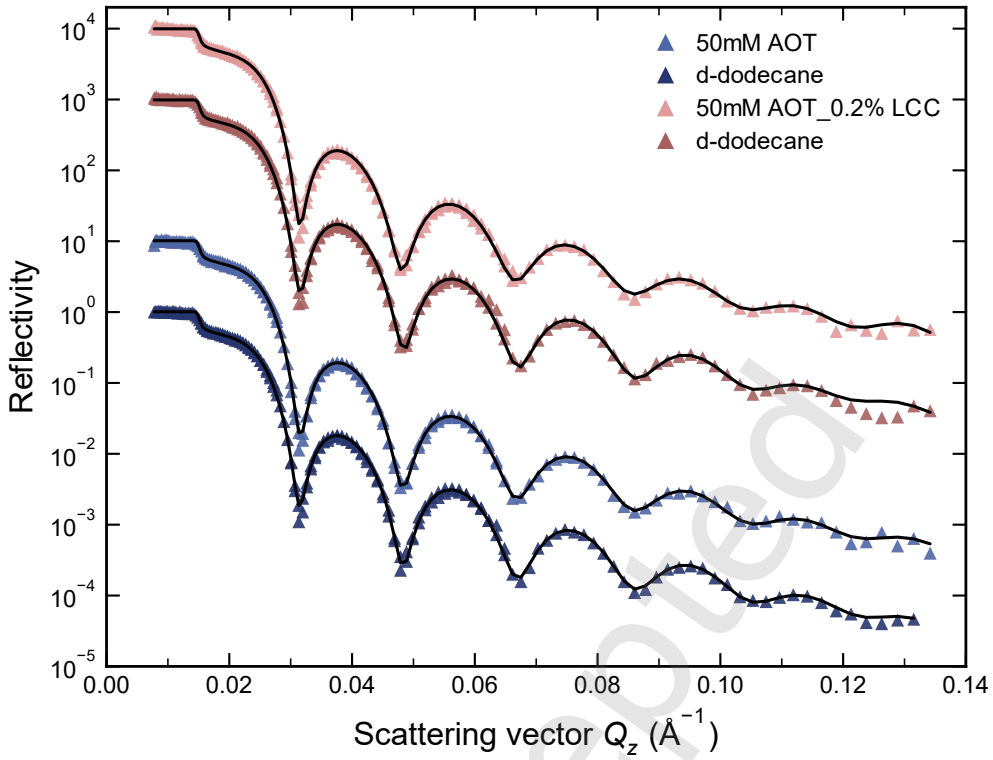

Fig. 8. Experimental and fitted neutron reflectivity curves of the AOT reverse micellar system before and after the addition of LCC.

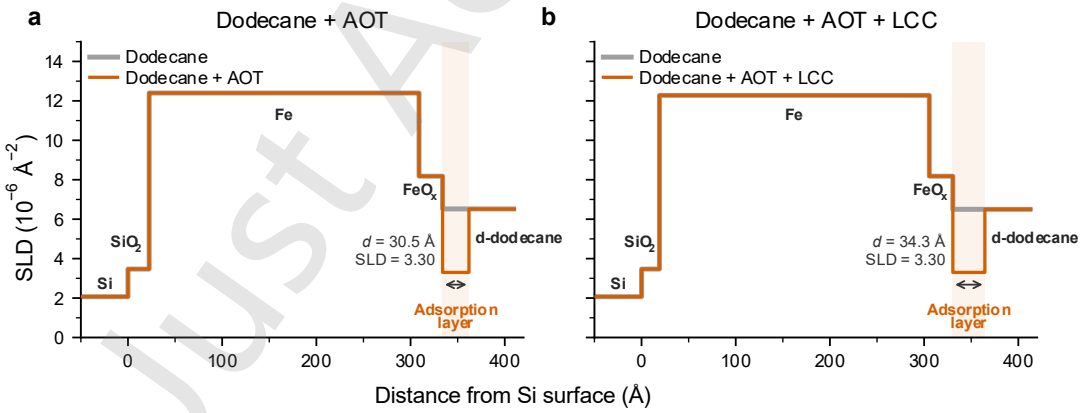

Fig. 9. Corresponding SLD profiles obtained from fitting. Comparison of the interfacial structural parameters was used to evaluate the influence of LCC incorporation on the adsorbed layer.

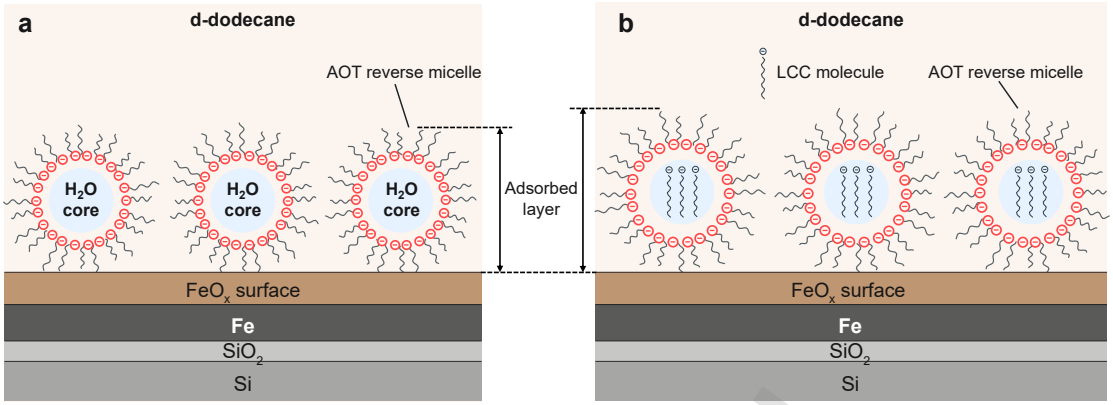

Fig. 10. Schematic illustration of the LCC-induced change in the reverse-micelle-derived adsorption layer at the FeO_x/d-dodecane interface.

Table. 3. Fitted NR parameters of AOT reverse micellar adsorbed layers before and after LCC addition.

Sample	Thickness / nm	SLD / $\times 10^{-6}$ Å^{-2}
50mM AOT	3.05	3.3
0.2 wt% LCC added in 50mM AOT	3.43	3.3

3.6. Surface chemical analysis of worn surfaces

To further clarify the interfacial processes occurring during sliding, XPS was performed on the worn surfaces after the tribological tests, and the high-resolution spectra are shown in Fig. 11. The Fe 2p and S 2p spectra exhibited generally comparable features among the tested samples. As shown in Fig. 11(b), the Fe 2p region consisted mainly of metallic iron and oxidized iron species, while no pronounced LCC-induced change was observed in the S 2p spectra shown in Fig. 11(c). In contrast, although the overall O 1s line shapes in Fig. 11(a) were similar, quantitative fitting revealed a water-content-dependent redistribution of the oxygen species. At w = 5, addition of 0.2 wt% LCC increased the fitted area ratio of the –OH-associated component to Fe–O from 1.61 to 2.33. This condition-specific change may reflect the combined effects of the more highly hydrated reverse-micellar environment and LCC-derived interfacial film coverage, which increase the relative contribution of surface-associated oxygen species and/or attenuate the underlying lattice Fe–O signal. Because oxygen-containing organic species may overlap with the –OH region, the measured ratio is regarded as an apparent –OH-associated/Fe–O ratio rather than direct evidence for the formation of additional hydroxyl groups. Overall, the XPS results indicate no major alteration of the Fe- and S-related surface chemistry but reveal a subtle, water-content-dependent change in the relative oxygen contributions after LCC addition. A clear difference, however, was observed in the Cl 2p region. As shown in Fig. 11(d), no Cl signal was detected on the worn surfaces lubricated without LCC, whereas a distinct Cl 2p doublet appeared only for the samples containing LCC. Since the only source of chlorine in the present system is LCC, the detected Cl signal directly demonstrates that LCC-derived species were present on the worn surface after sliding. This result indicates that LCC-derived chlorine-containing species were delivered to the sliding interface and remained on the worn surface after rinsing.

These XPS results confirm the chemical consequence of LCC delivery to the sliding interface, but they do not directly reveal how the reverse micelles respond to mechanical stress or how the encapsulated LCC is released from the aggregates. To address this point, molecular dynamics simulations were further performed to examine the structural evolution of LCC-loaded AOT reverse micelles under confined shear. The simulations were used to evaluate whether the reverse micellar aggregates remain intact during sliding or undergo deformation, fragmentation, and additive release under high-pressure shear conditions. This analysis provides molecular-level support for the proposed reverse-micelle-assisted delivery process, in which AOT reverse micelles solubilize polar additives in the bulk oil phase and release additive-derived species at the sliding interface under tribological conditions.

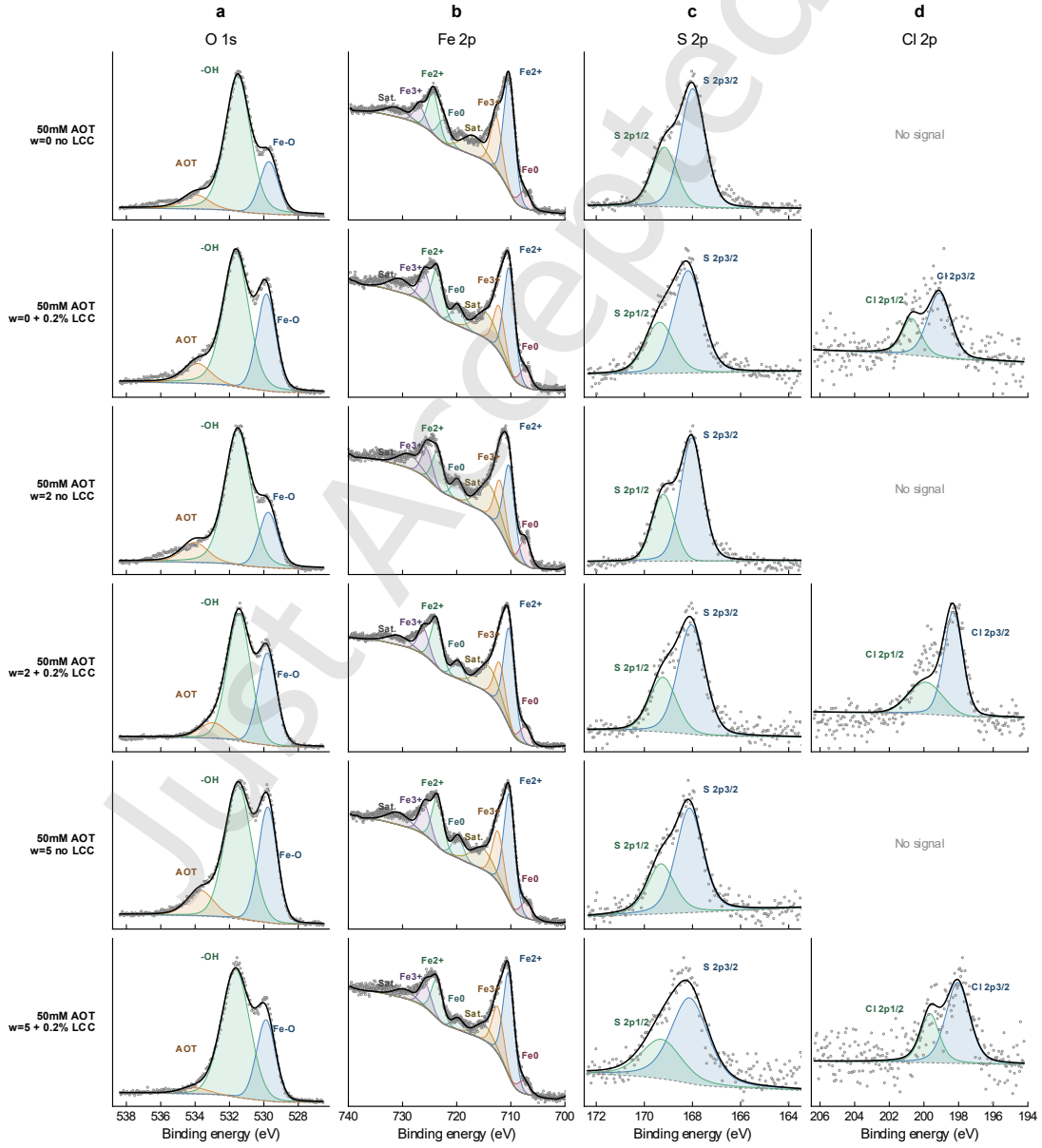

Fig. 11. XPS analysis of worn surfaces after tribological tests. High-resolution spectra of (a) O 1s, (b) Fe 2p, (c) S 2p, and (d) Cl 2p.

3.7. Molecular dynamics observation of reverse micelle disruption and LCC release

To visualize the structural response of LCC-loaded reverse micelles under sliding, representative MD trajectory snapshots were analyzed under the confined high-pressure shear geometry described above. In Fig. 12, the n-dodecane molecules are hidden for clarity, allowing the polar components of the reverse micelles to be observed more directly. The total number of molecules in the simulation cell remained constant throughout the simulation. At the beginning of the shearing trajectory, the AOT headgroups, water molecules, and LCC molecules were localized in compact reverse micellar aggregates. As shear proceeded, these initially compact aggregates became elongated, deformed, and gradually spread across the confined lubricant layer. The snapshots in Fig. 12 therefore indicate that the reverse micellar carrier structure can be mechanically disrupted under high-pressure sliding, exposing the incorporated LCC molecules to the surrounding interfacial environment.

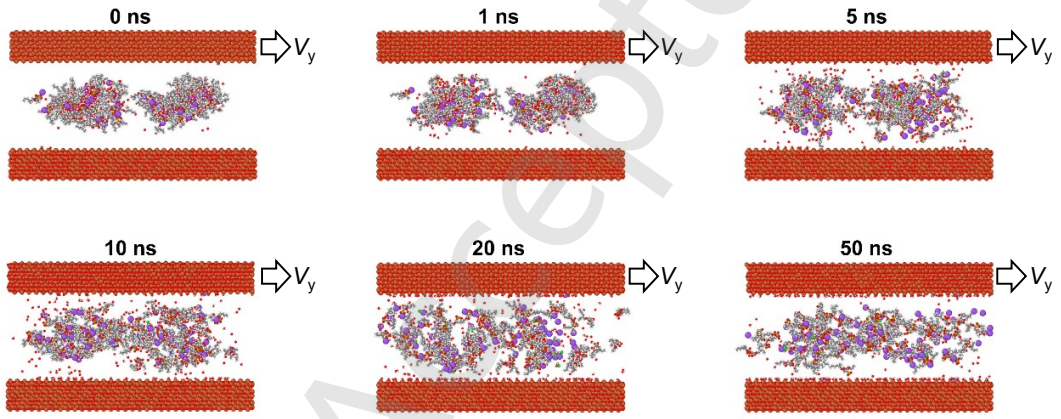

Fig. 12. Shear-induced disruption of LCC-loaded AOT reverse micelles observed by MD simulation. Representative snapshots at 0, 1, 5, 10, 20, and 50 ns show progressive deformation, expansion, and fragmentation of the initially compact reverse micellar aggregates between FeO_x slabs under 1 GPa and 20 m s^{-1} shear.

The disruption of the reverse micellar structure was further quantified using the metrics shown in Fig. 13, including integrity loss, core/headgroup expansion, cluster fragmentation, and spatial spreading. The retained fraction in Fig. 13a represents the fraction of water-core molecules or AOT headgroups that remained near the original reverse micelle core. Therefore, a decrease in this value indicates loss of the original micellar integrity. The retained fraction of the water core decreased from 0.97 in the first analyzed frame to an average of 0.16 over 40–50 ns and reached 0.13 at 50 ns. Similarly, the retained fraction of AOT headgroups decreased from 0.95 to an average of 0.29 over 40–50 ns and reached 0.27 at 50 ns. These results show that both the water core and the AOT headgroup region rapidly moved away from their initial compact micellar positions during shear.

The core/headgroup expansion was evaluated by the radius of gyration, Rg, as shown in Fig. 13b. Rg reflects the spatial size of each polar region; thus, an increase in Rg means that the initially compact core or headgroup domain became more extended. The water-core Rg

increased from 1.72 nm in the first analyzed frame to an average of 5.58 nm over 40–50 ns and reached 5.60 nm at 50 ns. Similarly, the AOT-headgroup Rg increased from 1.94 nm to an average of 4.90 nm over 40–50 ns and reached 5.12 nm at 50 ns. This expansion confirms that the polar domain was stretched and dispersed within the confined lubricant layer. In addition, the largest cluster fraction in Fig. 13c was used to evaluate cluster fragmentation. This value represents the fraction of polar components belonging to the largest connected cluster. The AOT^{+} water largest cluster fraction decreased sharply from 0.97 to 0.04, indicating that the initially connected polar aggregate fragmented into many smaller clusters. The spatial spreading shown in Fig. 13d further supports this interpretation, as the maximum spatial extents of the water-core and AOT–water regions increased during shear, showing that the fragmented polar components spread over a wider region in the confined film.

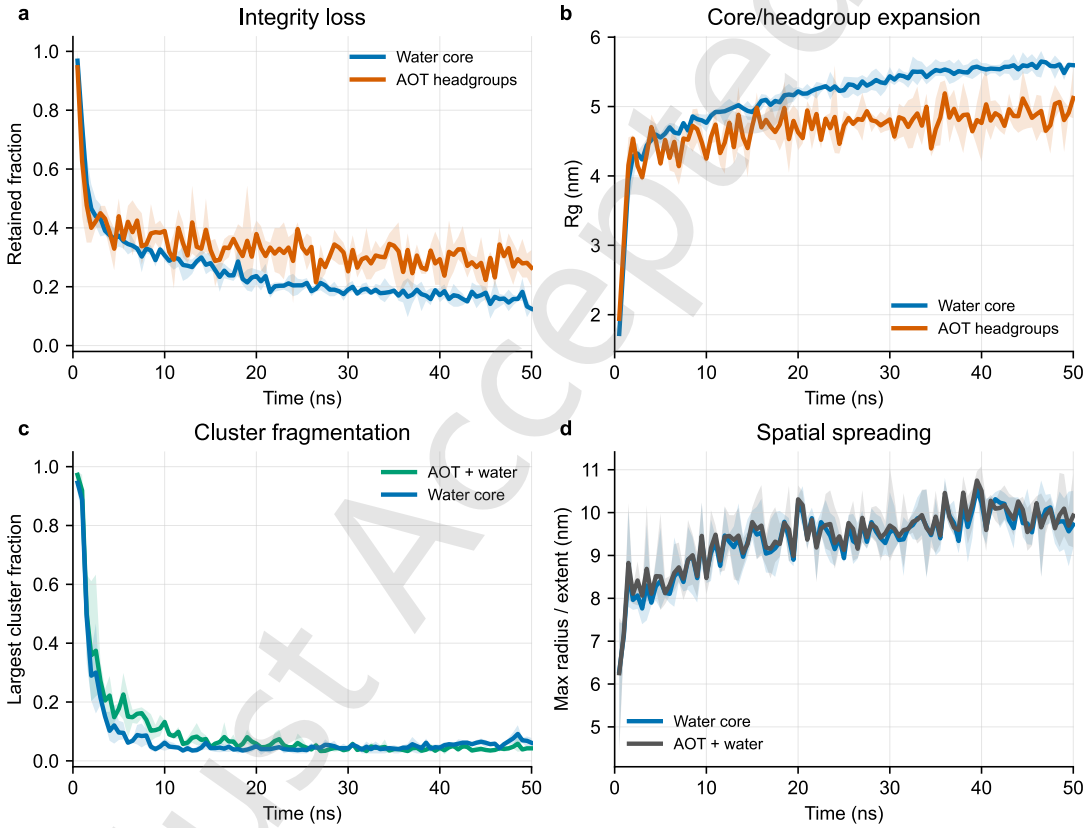

Fig. 13. Structural disruption of reverse micelles under high-pressure shear. Time evolution of reverse-micelle integrity during 50 ns sliding at 1 GPa and 20 m s^{-1}. (a) Retained fractions of water-core molecules and AOT headgroups within the original micelle region. (b) Radius of gyration of the water core and AOT headgroups. (c) Largest connected cluster fraction of water and AOT-water species. (d) Maximum spatial extent of the water core and AOT-water cluster. Lines show the mean of three initially defined reverse micelles; shaded regions indicate the range. The rapid loss of retained fraction, increase in Rg, collapse of cluster fraction, and growth of spatial extent indicate persistent micelle disruption during shear.

The LCC-specific behavior was analyzed separately, as shown in Fig. 14. The LCC retention in Fig. 14a describes the fraction of LCC headgroups retained near the original core. This value decreased from 0.94 in the first analyzed frame to an average of 0.18 over 40–50 ns and reached

0.11 at 50 ns, indicating that most LCC headgroups had moved away from their initial micellar environment by the end of the simulation. Consistently, the mean LCC headgroup–core distance shown in Fig. 14b increased from 1.84 nm in the first analyzed frame to an average of 5.04 nm over 40–50 ns and reached 4.99 nm at 50 ns. These values indicate that the LCC headgroups became substantially separated from the original reverse micelle cores during shear.

The contact analysis further confirms the weakening of interactions between LCC and the AOT reverse micellar structure. As shown in Fig. 14c, the number of LCC-sulfonate contacts decreased from 114 atom pairs in the first analyzed frame to an average of 26.7 atom pairs over 40–50 ns, with 45 atom pairs observed at 50 ns. Similarly, the number of LCC-AOT contacts in Fig. 14d decreased from 398 atom pairs to an average of 84.4 atom pairs over 40–50 ns, with 109 atom pairs observed at 50 ns. The local minima observed at approximately 42 ns represent transient fluctuations in the dynamic association between LCC and AOT. Therefore, the late-stage average, rather than the instantaneous minimum, was used to characterize the sustained reduction in contact numbers, while the values at 50 ns are provided as endpoint references. Because the LCC-sulfonate contacts reflect association with the main polar headgroup sites of AOT, whereas the total LCC-AOT contacts describe the overall association between LCC and AOT molecules, the mutually consistent decreases in these two metrics provide complementary evidence that LCC became progressively less associated with the AOT headgroup region during shear. Overall, the MD results show that LCC did not remain permanently trapped inside the initial reverse micellar cores. Instead, high-pressure shear caused integrity loss, core/headgroup expansion, cluster fragmentation, and spatial spreading of the reverse micellar aggregates, while promoting the separation of LCC headgroups from their original micellar environment.

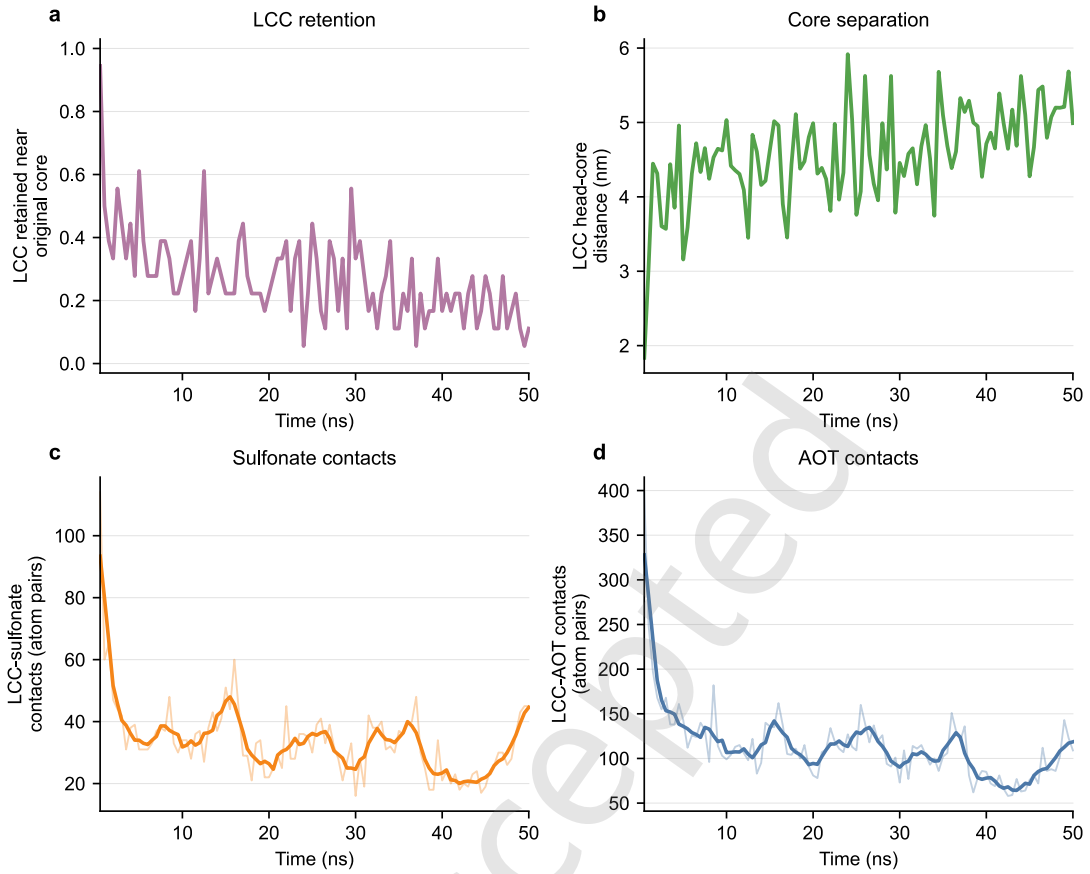

Fig. 14. LCC release metrics obtained from the LCC-containing MD trajectory. (a) Fraction of LCC headgroups retained near the original micelle core. (b) Mean distance between LCC headgroups and the tracked water-core center. (c) LCC-sulfonate contact count. (d) Total LCC-AOT contact count. The decrease in retention and contact numbers, together with the increase in headgroup-core distance, indicates progressive release of LCC from the original reverse micellar cores during shear.

To distinguish the respective contributions of normal loading and shear, additional load-only and shear-only control simulations were performed (Figs. S1 and S2). Under the load-only condition at 1 GPa, the reverse micelles largely retained their aggregate structures and no pronounced fragmentation was observed over 50 ns. In contrast, the shear-only simulation at 20 m/s produced substantial micellar deformation and disruption even in the absence of the externally applied normal load. These control simulations indicate that normal loading alone is insufficient to account for the micelle disruption observed in the production simulation and that lateral shear is the primary driving factor for the mechanically induced structural breakdown under the present simulation conditions.

3.8. Proposed lubrication mechanism of LCC-loaded reverse micelles

Combining the experimental and MD results gives a sequential delivery mechanism. In the bulk oil phase, AOT reverse micelles provide hydrated polar interiors that increase the apparent compatibility of LCC with non-polar dodecane. Under static conditions, NR shows that hydrated AOT aggregates adsorb at the FeOx/oil interface and that LCC incorporation increases the fitted adsorbed-layer thickness. Under sliding-like high-pressure shear in MD, the initially

compact LCC-loaded aggregates lose their original integrity, the polar core/headgroup region expands and fragments, and LCC headgroups move away from the original core.

The MD simulations establish that high-pressure shear can break down the reverse micellar carrier and liberate LCC from its original polar environment. This structural release step helps explain how a polar additive initially stabilized inside reverse micelles can become available for subsequent interfacial adsorption or retention at the sliding interface, as supported by the friction reduction and Cl 2p signal observed by XPS.

4. Conclusion

This study demonstrates that AOT reverse micelles can act as nanocarriers for introducing the polar friction modifier LCC into non-polar dodecane. Visual solubilization tests and DLS showed that increasing *w* expanded the polar reverse micellar environment and improved the apparent incorporation of LCC. NR contrast measurements further showed that hydrated AOT aggregates formed an adsorbed layer at the FeOx/oil interface, and LCC addition increased the fitted adsorbed-layer thickness from 3.05 to 3.43 nm under the same fixed-SLD fitting condition.

Tribological tests showed that the LCC-containing reverse micellar systems reduced friction relative to the corresponding AOT-only systems, with the largest experimental reduction observed at $w = 5$. XPS detected chlorine-containing LCC-derived species only on surfaces lubricated with LCC-containing formulations. This result indicates that LCC was delivered to the sliding interface and that LCC-derived species were retained on the worn surface after sliding.

The MD simulations further provided molecular-level evidence for the dynamic release process. Under 1 GPa and 20 m s^{-1} shear, the LCC-loaded reverse micelles underwent pronounced integrity loss, accompanied by expansion and fragmentation of the water-core/AOT-headgroup region and spatial spreading within the confined lubricant layer. Meanwhile, the LCC headgroups progressively separated from the original micelle cores, as indicated by decreased LCC retention, increased core separation, and reduced LCC–AOT contacts. Together, these results support a reverse-micelle-assisted delivery mechanism in which AOT aggregates solubilize the model polar additive in the bulk oil and adsorb at the interface; under sliding, disruption of the reverse micellar structure releases the incorporated additive, which subsequently participates in interfacial adsorption and leaves additive-derived chlorine-containing species on the worn surface.

Acknowledgments

This research was supported by the JSPS DC2 Fellowship (Grant No. 24KJ1406) and JSPS KAKENHI (Grant No. 23H05448). The authors sincerely thank Professor Masahiro Hino from the Institute for Integrated Radiation and Nuclear Science, Kyoto University, for his valuable assistance in preparing the Fe films employed in the neutron reflectometry experiments. The neutron experiment at the Materials and Life Science Experimental Facility of the J-PARC was performed under a user program (Proposal No. 2025MP-S002). Computation time was provided by the SuperComputer System, Institute for Chemical Research, Kyoto University.

References

[1] Nosonovsky M, Bhushan B. Green tribology: principles, research areas and challenges. Philos Trans A Math Phys Eng Sci 2010;368:4677–94. https://doi.org/10.1098/rsta.2010.0200.
[2] Holmberg K, Erdemir A. Influence of tribology on global energy consumption, costs and emissions. Friction 2017;5:263–84. https://doi.org/10.1007/s40544-017-0183-5.
[3] Holmberg K, Erdemir A. The impact of tribology on energy use and CO2 emission globally and in combustion engine and electric cars. Tribology International 2019;135:389–96. https://doi.org/10.1016/j.triboint.2019.03.024.
[4] Ijaz Malik MA, Kalam MA, Mujtaba MA, Almomani F. A review of recent advances in the synthesis of environmentally friendly, sustainable, and nontoxic bio-lubricants: Recommendations for the future implementations. Environmental Technology & Innovation 2023;32:103366. https://doi.org/10.1016/j.eti.2023.103366.
[5] Bhushan, B, Ko, PL. Introduction to Tribology. Applied Mechanics Reviews, vol. 56, 2003, p. B6–7. https://doi.org/10.1115/1.1523360.
[6] Meng Y, Xu J, Jin Z, Prakash B, Hu Y. A review of recent advances in tribology. Friction 2020;8:221–300. https://doi.org/10.1007/s40544-020-0367-2.
[7] Huang L, Eli W. Synthesis and Performance Study of a New Ether-Polyalphaolefin Base Oil. Lubricants 2025;13:404. https://doi.org/10.3390/lubricants13090404.
[8] Benda R, Bullen J, Plomer A. Synthetics basics: Polyalphaolefins — base fluids for high-performance lubricants. Journal of Synthetic Lubrication 1996;13:41–57. https://doi.org/10.1002/jsl.3000130105.
[9] Tormos B, Bermúdez V, Balaguer A, Giménez E. Compatibility Study of Polyamide (PA6) with Lubricant Bases for Electric Vehicle Applications. Lubricants 2024;12:54. https://doi.org/10.3390/lubricants12020054.
[10] Spikes H. Friction Modifier Additives. Tribol Lett 2015;60:5. https://doi.org/10.1007/s11249-015-0589-z.
[11] Fry BM, Moody G, Spikes HA, Wong JSS. Adsorption of Organic Friction Modifier Additives. Langmuir 2020;36:1147–55. https://doi.org/10.1021/acs.langmuir.9b03668.
[12] He X, Lu J, Desanker M, Invergo AM, Lohr TL, Ren N, et al. Boundary Lubrication Mechanisms for High-Performance Friction Modifiers. ACS Appl Mater Interfaces 2018;10:40203–11. https://doi.org/10.1021/acsami.8b11075.
[13] Zang C, Zhang Z, Fan X, Zhu M. Optimization of PAO/ester lubricant blends to enhance lubrication performance. Tribology International 2026;214:111201. https://doi.org/10.1016/j.triboint.2025.111201.
[14] Fernández Rico JE, Hernández Battez A, García Cuervo D. Wear prevention characteristics of binary oil mixtures. Wear 2002;253:827–31. https://doi.org/10.1016/S0043-1648(02)00229-6.
[15] Buzolic JJ, Li H, Aman ZM, Silvester DS, Atkin R. Surface-active ionic liquids as lubricant additives to hexadecane and diethyl succinate. Colloids and Surfaces A: Physicochemical and Engineering Aspects 2024;699:134669. https://doi.org/10.1016/j.colsurfa.2024.134669.
[16] Li H, Somers AE, Rutland MW, Howlett PC, Atkin R. Combined Nano- and Macrotribology Studies of Titania Lubrication Using the Oil-Ionic Liquid Mixtures. ACS Sustainable Chem Eng 2016;4:5005–12. https://doi.org/10.1021/acssuschemeng.6b01383.

[17] Gu H, Hirayama T. Encapsulation of lubricant additives − Enhanced lubrication performance through micellar solubilization of poorly soluble additives by surfactants. Tribology International 2025;210:110786. https://doi.org/10.1016/j.triboint.2025.110786.
[18] Zulauf Martin, Eicke HFriedrich. Inverted micelles and microemulsions in the ternary system water/aerosol-OT/isooctane as studied by photon correlation spectroscopy. J Phys Chem 1979;83:480–6. https://doi.org/10.1021/j100467a011.
[19] Eastoe J, Hollamby MJ, Hudson L. Recent advances in nanoparticle synthesis with reversed micelles. Advances in Colloid and Interface Science 2006;128–130:5–15. https://doi.org/10.1016/j.cis.2006.11.009.
[20] Eskici G, Axelsen PH. The Size of AOT Reverse Micelles. J Phys Chem B 2016;120:11337–47. https://doi.org/10.1021/acs.jpcb.6b06420.
[21] Gochman-Hecht H, Bianco-Peled H. Structure of AOT reverse micelles under shear. Journal of Colloid and Interface Science 2005;288:230–7. https://doi.org/10.1016/j.jcis.2005.02.083.
[22] Gu H, Hirayama T, Yamashita N, Okano T, Xu J, Sato N, et al. Tribological performance of a surfactant derived from its structure of molecular aggregates in water. Tribology International 2023;188:108881. https://doi.org/10.1016/j.triboint.2023.108881.
[23] Gu H, Hirayama T, Yamashita N, Xu J, Yamada M. Relationship between friction reduction effect and solubility in base oil of organic friction modifiers. Tribology International 2025;202:110304. https://doi.org/10.1016/j.triboint.2024.110304.
[24] Gu H, Hirayama T. Effect of surfactant self-assembly on lubrication performance in oil-based systems: the role of reverse micelles and vesicles. Front Mech Eng 2025;11. https://doi.org/10.3389/fmech.2025.1608716.
[25] Song X, Guo Z, Song Y, Zhang J, Gu H, Yamashita N, et al. Terminal group engineering of polyether amines: Overcoming steric hindrance for enhanced adsorption and lubrication performance on iron surfaces. Colloids and Surfaces A: Physicochemical and Engineering Aspects 2025;726:138099. https://doi.org/10.1016/j.colsurfa.2025.138099.
[26] Yamada NL, Torikai N, Mitamura K, Sagehashi H, Sato S, Seto H, et al. Design and performance of horizontal-type neutron reflectometer SOFIA at J-PARC/MLF. Eur Phys J Plus 2011;126:108. https://doi.org/10.1140/epjp/i2011-11108-7.
[27] Hino M, Oda T, Kitaguchi M, Yamada NL, Tasaki S, Kawabata Y. The ion beam sputtering facility at KURRI: Coatings for advanced neutron optical devices. Nuclear Instruments and Methods in Physics Research Section A: Accelerators, Spectrometers, Detectors and Associated Equipment 2015;797:265–70. https://doi.org/10.1016/j.nima.2015.06.046.
[28] Glavic A, Björck M. GenX 3: the latest generation of an established tool. J Appl Cryst 2022;55:1063–71. https://doi.org/10.1107/S1600576722006653.
[29] Abraham MJ, Murtola T, Schulz R, Páll S, Smith JC, Hess B, et al. GROMACS: High performance molecular simulations through multi-level parallelism from laptops to supercomputers. SoftwareX 2015;1–2:19–25. https://doi.org/10.1016/j.softx.2015.06.001.
[30] Martínez L, Andrade R, Birgin EG, Martínez JM. PACKMOL: A package for building initial configurations for molecular dynamics simulations. Journal of Computational Chemistry 2009;30:2157–64. https://doi.org/10.1002/jcc.21224.
[31] Jorgensen WL, Maxwell DS, Tirado-Rives J. Development and Testing of the OPLS All-Atom Force Field on Conformational Energetics and Properties of Organic Liquids. J Am

Chem Soc 1996;118:11225–36. https://doi.org/10.1021/ja9621760.

[32] Dodda LS, Cabeza de Vaca I, Tirado-Rives J, Jorgensen WL. LigParGen web server: an automatic OPLS-AA parameter generator for organic ligands. Nucleic Acids Res 2017;45:W331–6. https://doi.org/10.1093/nar/gkx312.

[33] Mat'usová A, Moody G, Dowding PJ, Eastoe J, Camp PJ. Experimental and simulation study of reverse micelles formed by aerosol-OT and water in non-polar solvents. Phys Chem Chem Phys 2024;26:27772–82. https://doi.org/10.1039/d4cp03389b.

[34] Jorgensen WL, Chandrasekhar J, Madura JD, Impey RW, Klein ML. Comparison of simple potential functions for simulating liquid water. J Chem Phys 1983;79:926–35. https://doi.org/10.1063/1.445869.

[35] Hess B, Bekker H, Berendsen HJC, Fraaije JGEM. LINCS: A linear constraint solver for molecular simulations. Journal of Computational Chemistry 1997;18:1463–72. https://doi.org/10.1002/(SICI)1096-987X(199709)18:12%3C1463::AID-JCC4%3E3.0.CO;2-H.

[36] Bussi G, Donadio D, Parrinello M. Canonical sampling through velocity rescaling. J Chem Phys 2007;126:014101. https://doi.org/10.1063/1.2408420.

[37] Bernetti M, Bussi G. Pressure control using stochastic cell rescaling. J Chem Phys 2020;153:114107. https://doi.org/10.1063/5.0020514.